SCIENCE CHINA
Information Sciences

• RESEARCH PAPER •
Special Focus on Brain Machine Interfaces and Applications

April 2022, Vol. 65 140404:1–140404:16
https://doi.org/10.1007/s11432-021-3392-1

Amplitude-frequency-aware deep fusion network for optimal contact selection on STN-DBS electrodes

Linxia XIAO[1†], Caizi LI[2†], Yanjiang WANG[1], Weixin SI[2*], Hai LIN[3,4],
Doudou ZHANG[3,4], Xiaodong CAI[3,4] & Pheng-Ann HENG[5,2]

[1]*College of Control Science and Engineering, China University of Petroleum (East China), Qingdao* 266580*, China;*
[2]*Shenzhen Institute of Advanced Technology, Chinese Academy of Sciences, Shenzhen* 518055*, China;*
[3]*Department of Neurosurgery, Shenzhen Second People's Hospital, Shenzhen* 518035*, China;*
[4]*School of Medicine, Shenzhen University, Shenzhen* 518000*, China;*
[5]*Department of Computer Science and Engineering, The Chinese University of Hong Kong, Hong Kong* 999077*, China*

Received 13 August 2021/Revised 27 October 2021/Accepted 17 December 2021/Published online 10 March 2022

Abstract Parkinson's disease (PD) is treated effectively by deep brain stimulation (DBS) of the subthalamic nucleus (STN), using an electrode inserted into the head of a PD patient. The electrode has multiple electrical contacts along its length, so the best may be chosen for selectively stimulating the STN. Neurosurgeons usually determine the optimal stimulated contact via the clinical experience of the neurosurgeon and the motor improvement of PD patients. This is a time-consuming and labor-intensive trial-and-error process. The selection of optimal stimulated contact highly depends on the locations of sweet spots, which are manually identified by the characteristic features of microelectrode recordings (MERs). This paper presents an amplitude-frequency-aware deep fusion network for optimal contact selection on STN-DBS electrodes. The method first obtains the amplitude-frequency fusion features by combining the MERs time sequence features and the amplitude sequence features, and then uses the convolutional neural network (CNN) with convolutional block attention module (CBAM) to identify both the border of the STN and the sweet spots to implant the electrode. The optimal stimulated contact can be selected according to the distribution of the sweet spots. Experimental results indicate that, for successful surgeries, neurosurgeons and the proposed AI solution selected the same optimal contacts. Furthermore, the proposed method outperforms the state-of-the-art methods for STN and sweet spot identification. The proposed method shows great potential for optimal contact selection to improve the efficiency of STN-DBS surgery and reduce the dependence on clinicians' experience.

Keywords optimal contact selection, sweet spots, microelectrode recordings, amplitude-frequency feature, deep fusion network

Citation Xiao L X, Li C Z, Wang Y J, et al. Amplitude-frequency-aware deep fusion network for optimal contact selection on STN-DBS electrodes. Sci China Inf Sci, 2022, 65(4): 140404, https://doi.org/10.1007/s11432-021-3392-1

1 Introduction

Parkinson's disease (PD) is a common progressive neurodegenerative disease that leads to motor symptoms, such as uncontrollable shaking, stiffness, walking difficulties, and lack of coordination, severely impacting the quality of life of patients [1]. Deep brain stimulation (DBS) has been applied in the field of neuromodulation for the treatment of neurodegenerative diseases. DBS consists of microelectrode recording (MERs) monitoring, electrode implantation, and optimal electrode contact stimulation. Accurate electrical stimulation of the target region leads to brain penetration effects [2], which can reduce the symptoms of patients with PD. Subthalamic nucleus (STN)-DBS surgery has become a popular technique for the treatment of PD patients [3]; however, the outcome of STN-DBS surgery is highly dependent on electrical stimulation at the optimal electrode contact [4, 5]. In order to select the optimal

---

[*] Corresponding author (email: wx.si@siat.ac.cn)
[†] Xiao L X and Li C Z have the same contribution to this work.

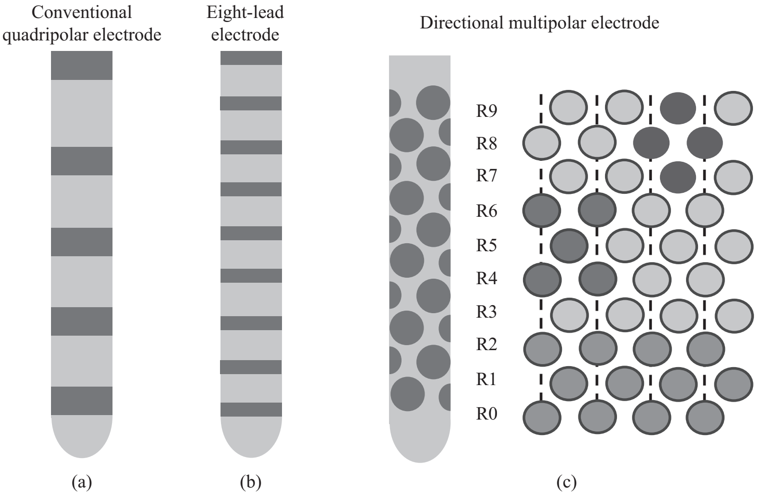

Figure 1 Examples of electrodes with multiple contacts. (a) Conventional quadripolar electrode; (b) eight-lead electrode; (c) directional multipolar electrode.

contact on the electrode, clinicians should first determine where to implant the therapeutic electrode by identifying the border of the STN through electrophysiological activities. After electrode implantation, all possible contact positions are determined; selecting the optimal one is a difficult task for clinicians. In the clinic, neurosurgeons adopt a trial-and-error strategy to observe the motor improvement of patients for each contact, which is time-consuming and labor-intensive, especially when more complex electrodes with multiple contacts [6, 7], as shown in Figure 1, are applied. Such electrodes are projected to replace conventional quadripolar electrodes in the near future. Therefore, there is an urgent need to develop an effective method of optimal stimulated contact selection on the STN-DBS electrode; such a method could reduce the duration of surgery and dependence on clinicians' experience.

Note that the STN is functionally composed of sensorimotor, associative, and limbic regions [8, 9], and the optimal contact is localized in the patient-specific sensorimotor region of PD patients [10]. Because the sensorimotor region of the STN is a very small region, the sweet spot accumulation can be regarded as the sensorimotor region of STN, which can be used to assist clinicians in selecting the optimal contact accurately and efficiently [11]. Moreover, the location of the electrode placement can also affect the optimal stimulated contact selection. Therefore, electrode location and optimal stimulated contact selection are indispensable for the success of STN-DBS surgery.

MERs are used to monitor electrophysiological activities in the brain. They provide an effective means to identify the border of the STN and the sweet spots for STN-DBS surgery. As each part of the brain has unique electrophysiological activities, each structure of the brain can be distinguished by the features of MERs [12]. In recent years, many techniques have been proposed to classify MERs according to the time sequence features for STN detection [13]. Karthick et al. [14] proposed using wavelet features of MERs data and random forest (RF) to identify the STN. Khosravi et al. [15] proposed a combination of wavelet transformation features and a convolutional neural network (CNN) classifier to automatically identify the STN and its borders using MERs data. Although these methods can identify the border of the STN to determine the electrode location for clinicians, an effective method of selecting the optimal stimulated contact based on the precise location of the electrode is needed. Clinicians make this selection according to the presence of sweet spots within the STN identified from the MERs data [16, 17]. Xiao et al. [18] proposed a method of automatic sweet spots identification by employing the Gramian angular summation field (GASF) features to classify the MERs. The GASF method is a commonly used amplitude sequence feature extraction method [19]; it takes time-series data and converts it to an image for better AI classification. In general, GASF images do not show obvious stripe features to represent the high-frequency and high-amplitude parts of the MERs signals, and the time sequence feature extraction method is unfavorable for the MERs signals with unobvious spikes. Therefore, all the above-mentioned methods analyze either only the time sequence features or the amplitude sequence features for classifying the MERs data; a method that analyzes both is desirable for clinical applications. Moreover, neurosurgeons identify the STN border and sweet spots via the fusion features of the amplitude sequence and time sequence, in order to decide precisely where to insert the electrode and which contacts on the electrode should be stimulated. There is presently no learning algorithm that does this.

As mentioned above, neurosurgeons determine the electrode locations according to the border of the STN identified from the MERs, and then determine the optimal stimulated contact via a trial-and-error strategy. Specifically, the MERs are manually graded by experienced clinicians according to the spike, frequency, and amplitude features. The clinicians mark the sweet spots with higher grades [20], and the optimal stimulated contact can be selected according to sweet spot accumulation [4]. This work proposes an amplitude-frequency-aware deep fusion network for optimal stimulated contact selection on STN-DBS electrodes. The method first identifies the border of the STN to indicate where to implant the permanent electrode, and then the method identifies sweet spot accumulation to assist clinicians in selecting the optimal stimulated contact.

The main contributions of this work can be summarized as follows.

(1) 2D time sequence images and GASF images were employed to represent the high-frequency and high-amplitude features, respectively, of MERs time-series signals. This allowed the AI to effectively extract the anomalous features indicating sweet spots.

(2) The amplitude-frequency-aware deep fusion network was applied to automatically grade the MERs signals according to the different frequencies and amplitudes. This could assist clinicians in efficiently identifying the STN border and sweet spots.

(3) An automatic decision-making method was presented for the intra-operative and post-operative STN-DBS surgery. The method accurately identified both the STN border for electrode location and the sweet spots for optimal stimulated contact selection.

2 Method

The entire process is summarized in two stages: (1) automatic analysis of intra-operative MERs and (2) optimal stimulated contact selection. To address the problem of extracting features from the discontinuous high-frequency and high-amplitude MERs signals, as well as the MERs signals with unobvious spikes, an amplitude-frequency-aware deep fusion network was developed. This network provided an auxiliary AI solution for the intra-operative and post-operative decision-making for STN-DBS surgery, including the location of the STN border and sweet spots, and the determination of the optimal stimulated contact on the electrode. First, the amplitude-frequency-aware fusion feature images of MERs were obtained. This was done by combining the time sequence features extracted by continuous wavelet transform (CWT) and the amplitude sequence features generated by GASF. CNN was then used with convolutional block attention module (CBAM) [21] model to detect amplitude-frequency-aware fusion features, to identify the non-STN, sweet spots of STN, and non-sweet spots of STN. After the border of the STN is identified, the DBS electrode can be implanted to contact the dorsal border. Finally, the optimal stimulated contact was determined according to the electrode location and distribution of the sweet spots. A block diagram of the method is shown in Figure 2.

2.1 Materials

The present study was approved by the local ethics committee of the hospital for human research. Written informed consent was obtained from all participants after a full explanation of the procedures involved. The dataset contained a total of 7420 MERs signals from 200 successfully executed STN-DBS surgeries performed on 100 PD patients since January, 2018. The STN-DBS surgeries involved implanting bipolar electrodes. The MERs signals were collected using an electrophysiological navigation system (NeuroNav 223/12, Alpha Omega Engineering, Israel) in one medical center.

The MERs signals were recorded using one or two implanted tungsten microelectrodes. DBS microelectrodes were implanted along the planning electrode trajectory by neurosurgeons. Typically, MERs measurements were taken as follows:

(1) The microelectrode (cannula with stylet) was inserted down to 10 mm above the estimated target.

(2) The microelectrode was further inserted to 5 mm in 1 mm (approximately) steps, and a MERs signal was measured at each step.

(3) The microelectrode was backed off again in 0.5 mm steps, the MERs signal being measured at each step.

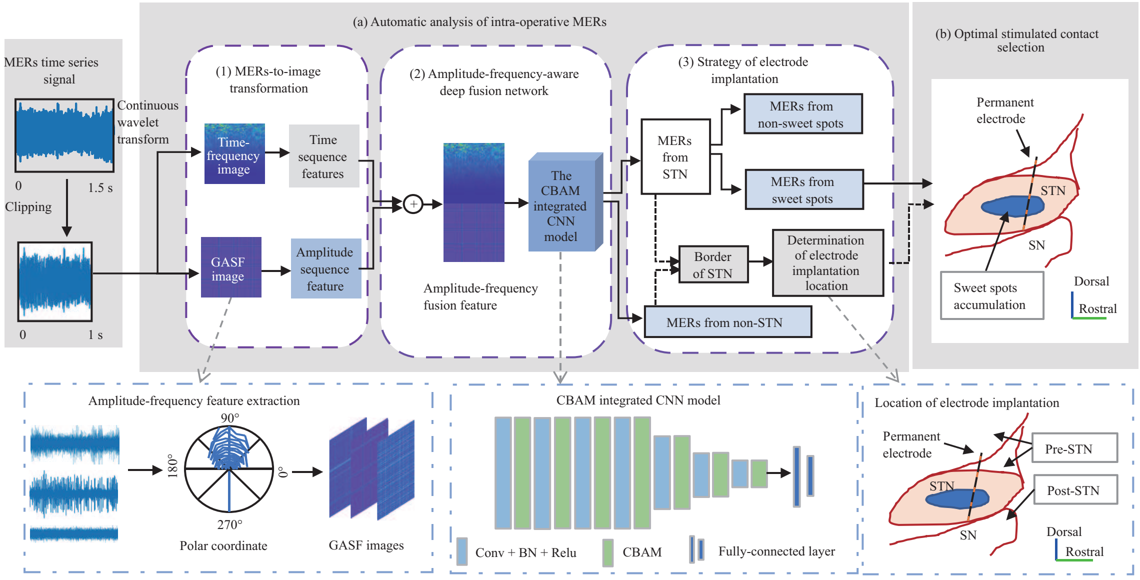

Figure 2 (Color online) Block diagram of the proposed method. (a) Automatic analysis of intraoperative MERs; (b) optimal stimulated contact selection. The first stage contains (1) MERs-to-image transformation, (2) amplitude-frequency-aware deep fusion network, and (3) strategy of electrode implantation. $\oplus$ indicates that the amplitude-frequency fusion feature was generated by concatenating the time sequence and amplitude sequence features. The post-STN represents the region from the scalp to the ventral border, and the pre-STN represents the region from the ventral border to the SN.

The microelectrode movement may introduce noise into the measured signal. This noise decays after several seconds. To allow the signals time to stabilize, approximately 1–5 s of raw MERs data were collected by the clinicians at each position of the electrode. Signals with longer time durations would bias the algorithm; therefore, following the suggestion of professional neurosurgeons, a 1-s segment of least-noisy data was selected from each MERs signal [22, 23]. These MERs segments were labelled by professional neurosurgeons with the Mapfile converter (Copyright Alpha Omega 2018, Version 5.1.11.0). All signals were sampled at 24 kHz, amplified 1000 times, digitally band-pass filtered in MATLAB (Mathworks, Inc., Natick, MA) [15,23,24] with a 6-pole Butterworth filter between 0.5 and 5 kHz and a notch filter of 60 Hz. All raw MERs signals were then downsampled to 12 kHz with an appropriate antialiasing filter [14], which reduced the number of data points and improved the operational efficiency of the neural network. The microelectrode typically passes through the following structures of the brain: reticular thalamic nucleus (Rt), inter capsule (IC), zona incera (ZI), H2 field of forel (H2), STN, and the substantia nigra (SN) [25], as shown in Figure 3. When the neurosurgeons determine the best trajectory and final location for the electrode, all the microelectrodes are removed, and the final quadripolar therapeutic electrode is inserted into the STN. In the postoperative stage, clinicians select the optimal electrode contact to improve motor symptoms according to clinical experience.

2.2 Automatic analysis of intra-operative MERs

During STN-DBS surgery, the microelectrode trajectory passes through the prefrontal motor cortex to the SN [25]. To avoid electrical stimulation in the SN, it is critical to select the correct location for electrode implantation. After the electrode has been implanted, the optimal stimulated contact can be selected according to the locations of the sweet spots. In this regard, the challenge of STN-DBS is to identify the border of the STN for electrode location and the sweet spots for optimal stimulated contact selection. Owing to the different features of MERs signals from different brain structures, the STN can be identified according to the features of MERs. These features include those with high-frequency, high-amplitude, spikes, and background characteristics. Experienced clinicians usually identify the sweet spots by first grading the MERs [20] according to the spike, frequency, and amplitude features. The MERs from the sweet spots belong to the highest two grades, and the rest are the MERs from non-sweet spots. The identification of sweet spots and the border of STN can be defined as a typical classification problem, namely, MERs from non-STN, sweet spots of STN, and non-sweet spots of STN. In this work, the analysis of intraoperative MERs was formulated as the following three steps: MERs-to-image transformation, amplitude-frequency-aware deep fusion network, and strategy of electrode implantation.

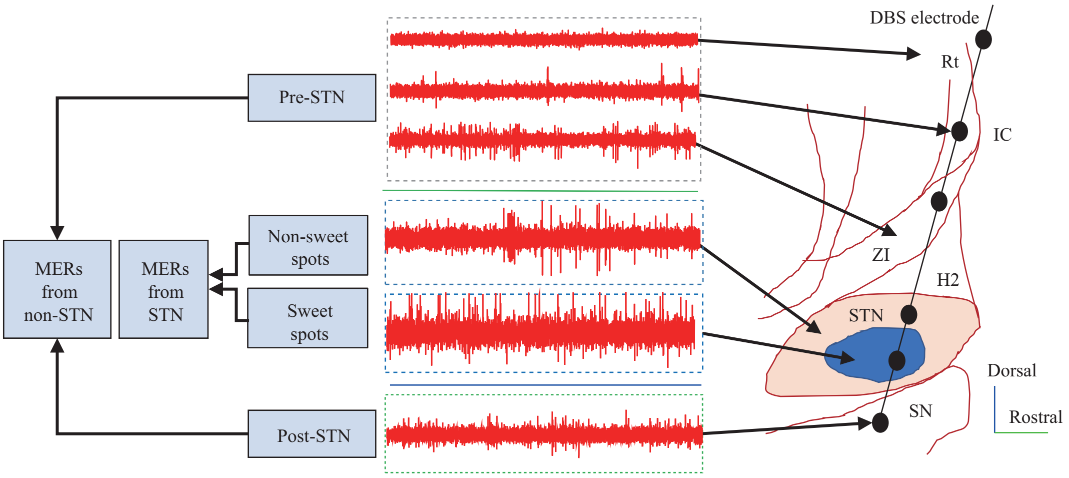

Figure 3 (Color online) The typical microelectrode tracks of STN-DBS surgery. The DBS electrode is implanted through Rt, IC, ZI, H2, STN, and SN, and the corresponding MERs signals of these structures are shown on the left side. The MERs signals come from STN (non-sweet spots of STN, sweet spots of STN) and non-STN (pre-STN and post-STN).

2.2.1 *MERs-to-image transformation*

Owing to the complex features of 1D MERs signals, including random, multi-component, and non-stationary features, 1D signals-to-2D images can overcome these difficulties for the MERs feature extraction by transforming the MERs signals into images. The MERs-to-image transformation can be conducted through two common feature extraction methods, including time sequence feature extraction and amplitude sequence feature extraction.

As for the time sequence features of MERs signals, the wavelet transform (WT) has the advantage of analyzing non-stationary signals, because the extracted wavelet coefficients provide the time frequency distribution of the MERs data [15, 26]. As a time frequency domain conversion method, CWT can be utilized to effectively extract the time sequence features to generate the time frequency spectrum images from MERs data. Given a time sequence signal $x(t)$, the CWT is expressed as

$$\psi_{a,b}(t) = \frac{1}{\sqrt{|a|}}\psi\left(\frac{t-b}{a}\right), \tag{1}$$

$$W(a,b) = \int_{-\infty}^{\infty} x(t)\psi_{a,b}(t)\mathrm{d}t, \tag{2}$$

where ψ is the wavelet basis function, a is the scaling coefficient that extends or reduces $\psi(t)$ to $\psi(t/a)$, $a \neq 0$, and b is the time-shift coefficient that specifies the location of the wavelet. Complex Morlet wavelet — a widely used wavelet basis function (cmor3-3) [27, 28] — was chosen on account of it having the optimal time-frequency resolution and the best focusing performance for the time sequence feature extraction in the CWT method. The longer length of the amplitude sequence leads to a higher frequency resolution, while an excessively long amplitude sequence may cause a loss of time resolution; therefore, the length of the amplitude sequence was set to 256. Because the sampling frequency f_s was 12 kHz, the sampling period was $1/f_s$, whereas the total duration of each signal was 1 s. The time-shift coefficient sequence was obtained by the sample time along the time axis. The wavelet coefficients were calculated by changing the time-shift coefficients to obtain the final time-frequency feature maps. As shown in Figure 4(a), the CWT, which is the typical time sequence feature extraction method, was used to generate time frequency images with dimensions 100×100×3. These images show the different frequency characteristics of the MERs from the various regions: sweet spots of STN, non-sweet spots of STN, and non-STN.

To obtain the amplitude sequence features of the MERs, the MERs data was converted into amplitude sequence visual images using the GASF method [18, 19]. Given an MERs time series $Y = \{y_1, y_2, \ldots, y_n\}$, Y was normalized to the interval $[-1, 1]$,

$$\tilde{y_i} = \frac{(y_i - \max(Y)) + (y_i - \min(Y))}{\max(Y) - \min(Y)}. \tag{3}$$

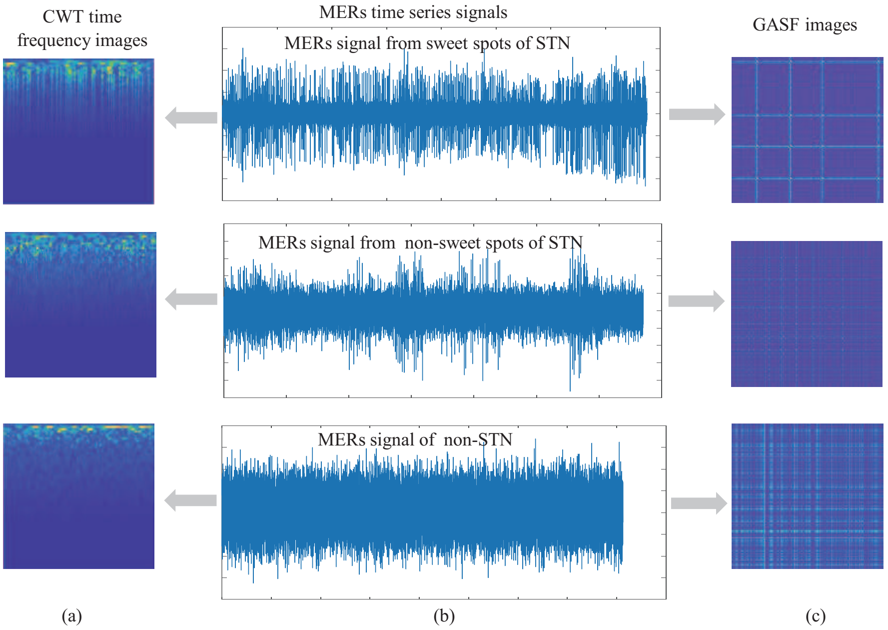

Figure 4 (Color online) Samples of MERs-to-image transformations. (a) CWT time-frequency images; (b) MERs time-series signals; (c) GASF images. The MERs signals are from sweet spots of STN, non-sweet spots of STN, and non-STN.

Then, the normalized MERs data were converted into polar coordinates,

$$\begin{cases} \phi_i = \arccos(\widetilde{y}_i), \\ r = \dfrac{t}{n}. \end{cases} \tag{4}$$

The value of the normalized MERs $\widetilde{y}_i$ and the corresponding time stamp t are expressed by the angle ϕ_i and radii r, where n is a constant factor that regularizes the span. The time correlation within different time intervals can be easily identified by examining the trigonometric sum. The GASF is represented as

$$\text{GASF} = [\cos(\phi_i + \phi_j)]. \tag{5}$$

The GASF matrix was converted into a GASF image with dimensions 100×100×3, as shown in Figure 4(c). Because of the obvious texture and stripe features in the converted GASF images generated from MERs, the GASF feature extraction method can be used to distinguish between sweet spots of STN, non-sweet spots of STN, and non-STN.

2.2.2 *Amplitude-frequency-aware deep fusion network*

In order to accurately identify the border of the STN and the sweet spots, the amplitude-frequency-aware fusion features were obtained. This was done by concatenating the time frequency images generated by CWT and amplitude sequence images generated by GASF, such that the dimension of the obtained amplitude-frequency-aware fusion feature maps was 100×100×6. The CBAM-integrated CNN model [21] was used for this task because the attention mechanism can focus on the amplitude-frequency-aware fusion features of the MERs signals and suppress the irrelevant neural activity features. This enables detection of the amplitude-frequency-aware fusion features for identifying the border of the STN and the sweet spots.

To simultaneously avoid the loss of information caused by pooling layers while extracting richer information for the classification task, several stages of convolution were performed with full resolution. Considering that the input size was set to 100×100, the receptive fields of neurons in the CNN after four stages were sufficient to cover the input. Pooling layers were employed in the last three stages to obtain the high-level features for the classification task. As shown in Figure 5, the network was composed of seven stages, and each stage contained a convolutional layer and a CBAM module. A fully connected layer followed by a softmax layer was employed to obtain the output. The maxpooling layer followed the fourth, fifth, and sixth stages. Each convolution layer was followed by batch normalization (BN) and a

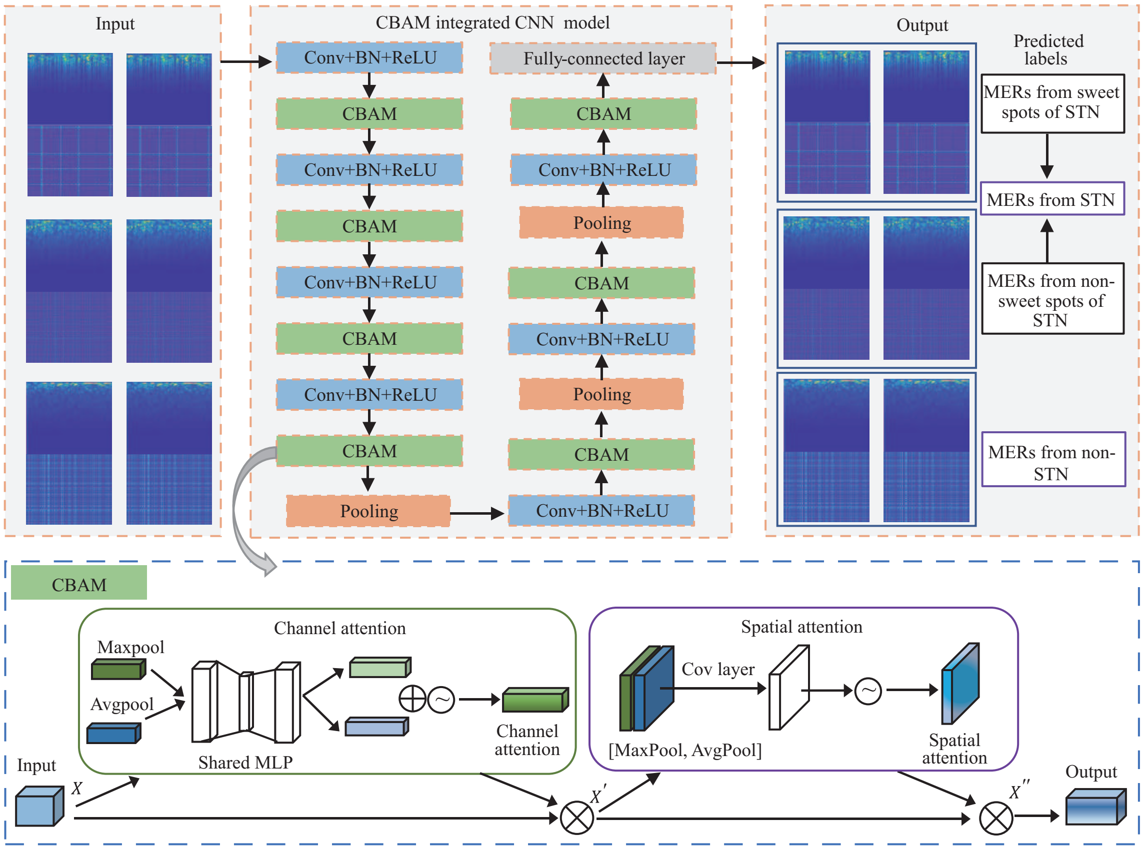

Figure 5 (Color online) The structure of the CBAM integrated CNN model. CBAM consists of a channel attention module and spatial attention module.

rectified linear unit (ReLU). The CBAM was composed of two main sub-modules applied in sequence: first, the channel attention module, and second, the spatial attention module. For the channel attention module, the input feature map went through both the average pooling and maximum pooling simultaneously, and then passesd through the multi-layer perceptron (MLP). The output features of the MLP were summed elementwise and then sent through the sigmoid activation function. Given an intermediate feature map X as the input, the formula of channel attention was calculated as

$$\begin{cases} M_C(X) = \sigma(\mathrm{MLP}(f_{\mathrm{AvgPool}}(X)) + \mathrm{MLP}(f_{\mathrm{MaxPool}}(X))), \\ X' = M_C(X) \otimes X, \end{cases} \tag{6}$$

where M_C denotes the channel attention module, and f_{AvgPool} and f_{MaxPool} indicate average pooling and maximum pooling, respectively. MLP represents the multilayer perceptron, σ is the sigmoid function, $\otimes$ represents element-by-element multiplication, and X' is the vector of features output by the channel attention module.

The output feature map of the channel attention module was taken as the input feature map of the spatial attention module. First, the input was processed through average pooling. Compressed sampling was conducted in the channel dimension, followed by a convolution layer to obtain the 2D spatial attention map. Spatial attention was calculated as

$$\begin{cases} M_S(X) = \sigma(F_{\mathrm{cov}}([f_{\mathrm{AvgPool}}(X); f_{\mathrm{MaxPool}}(X)])), \\ X'' = M_S(F) \otimes X', \end{cases} \tag{7}$$

where M_S denotes the spatial attention module, F_{cov} indicates the convolution operation, and X'' is the final output of the CBAM.

In the neural network, the number of channels of the convolutional layer in stages 1 to 7 were 16, 32, 64, 128, 128, 128, and 128, respectively. The kernel size of the convolutional layer was set to 3×3, and

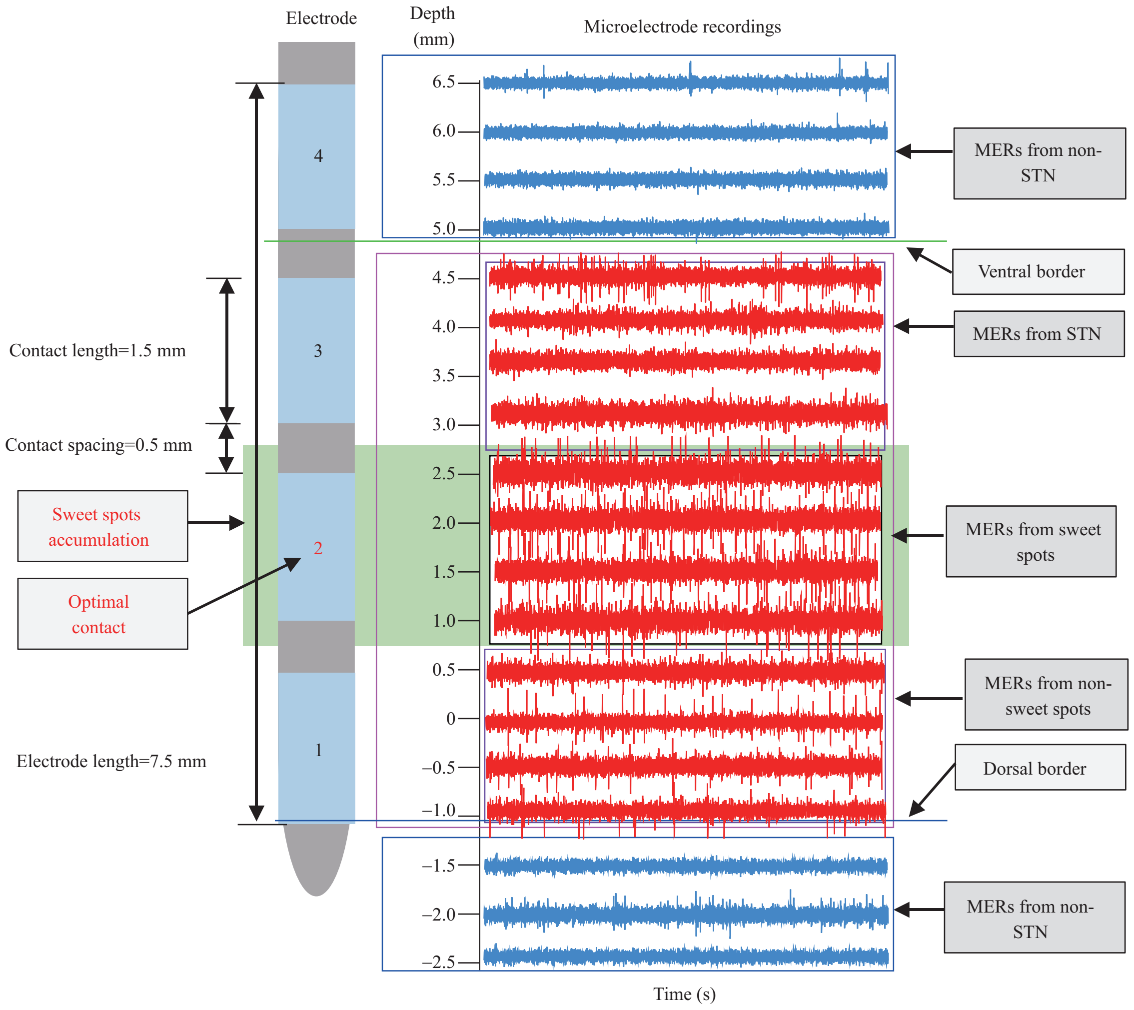

Figure 6 (Color online) The position of the implanted electrode and the selection of optimal stimulated contact. The blue and green lines represent the dorsal and ventral borders of the STN, respectively. The MERs signals from the STN and non-STN are marked in red and blue, respectively. The electrode contacts are labelled as 1, 2, 3, and 4. The depth of electrode implantation ranges from 6.5 mm above the estimated target to 2.5 mm below the estimated target. The MERs signals from the sweet and non-sweet spots are labelled in the black and purple rectangular boxes, respectively. The green-filled rectangle indicates the region of sweet spot accumulation. The optimal stimulated contact is marked in red.

the kernel size of the max pooling layer was 2×2. In the CBAM module, the convolutional kernel size was 7×7. The model was optimized using the Adam optimizer [29] and the network was initialized by “random_uniform”. The learning rate and batch size were set to 1e−2 and 32, respectively, and 50 epochs were chosen for training.

2.2.3 *Strategy of electrode implantation*

For electrode implantation during STN-DBS surgery, the accurate distinction between the STN and SN affords the optimal therapeutic benefits, while avoiding complications [25]. According to the characteristic features of MERs, the dorsal and ventral borders of the STN can be identified using the amplitude-frequency-aware feature fusion method. Figure 6 shows the electrode during the STN-DBS surgery. The length of the electrode was approximately 7.5 mm, and consisted of four 1.5 mm long contacts spaced by 0.5 mm. The size of the STN region was approximately 4–7 mm. Due to the limited length of the electrode, the need to impact the STN as much as possible, and the need to avoid stimulating the SN, the best location to implant the DBS electrode is close to the dorsal border of the STN, as shown in Figure 6.

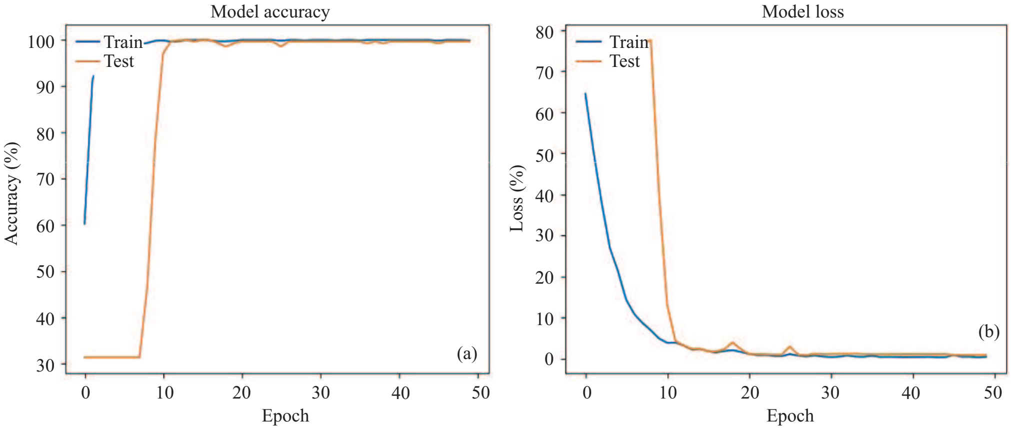

Figure 7 (Color online) The curves of the average training accuracy, testing accuracy and loss. The blue lines represent the training curves and the orange lines represent the testing curves. (a) The curves of the average training accuracy, testing accuracy of different epochs; (b) the curves of the average training loss, testing loss of different epochs.

2.3 Optimal stimulated contact selection

After electrode implantation, the optimal locations of the postoperative electrical stimulation (i.e., optimal contact) should be determined to improve the physical state of PD patients. Considering that sweet spot accumulation can be regarded as the sensorimotor region of STN [20], the optimal stimulated contact can be determined by the distribution of sweet spots. It is also very important to avoid stimulating the SN. As shown in Figure 6, the optimal stimulated contact was selected according to its proximity to the highest density of sweet spots [4].

2.4 Performance evaluation

These five evaluation criteria were employed for the performance evaluation of the amplitude-frequency-aware deep fusion network used for classification: accuracy ($\mathrm{Ac} = (\mathrm{TP} + \mathrm{TN})/(\mathrm{TP} + \mathrm{FP} + \mathrm{FN} + \mathrm{TN})$), precision ($\mathrm{Pre} = \mathrm{TP}/(\mathrm{TP} + \mathrm{FP})$), sensitivity (recall) ($\mathrm{Se} = \mathrm{TP}/(\mathrm{TP} + \mathrm{FN})$), specificity ($\mathrm{Sp} = \mathrm{TN}/(\mathrm{TN} + \mathrm{FP})$), and F1-score ($\text{F1-score} = (2 \times \mathrm{Pre} \times \mathrm{Se})/(\mathrm{Pre} + \mathrm{Se})$), where TP, FP, FN, TN represent true positive, false positive, false negative, and true negative, respectively. The F1-score was calculated according to the precision and sensitivity.

3 Results

In this study, the entire dataset contained 100 PD patients, from which 80 samples were randomly selected for training and 20 samples for testing. A 10-fold cross-validation was performed to evaluate the proposed method. For each fold, 10% of the samples were randomly selected from the training data for validation, and the rest were used for training. In the raw MERs preprocessing stage, the experiment was conducted using MATLAB 2017a on a Windows10 operating system. In the amplitude-frequency-aware deep fusion feature extraction and MERs identification, the experiment was performed on Ubuntu 16.04 with Keras 2.2.2, Python 3.7.6, and NVIDIA 1080Ti.

3.1 Quantitative analysis

The performance of the proposed method was evaluated in two classification problems: STN detection and sweet spot detection. To evaluate the performance of the proposed method, the method was compared with several classical methods for MERs classification. As shown in Figure 7, the loss curves demonstrate that the loss of the proposed model converges rapidly to zero at the end of the epochs, and the average training accuracy curves demonstrate that no overfitting occurs during the training stage.

STN detection analysis. For STN detection, machine learning methods, including k-nearest neighbors (KNN, $K = 5$), linear support vector machine (SVM), RF [14], and CNN [15] were the common classifiers used to identify the STN. Moreover, CWT and GASF were the common time sequence and amplitude sequence feature extraction methods, respectively. As mentioned, this work employed an

Table 1 Results of the proposed method with a 10-fold cross-validation for the identification of the STN (%)

Criteria	1	2	3	4	5	6	7	8	9	10	Results
Accuracy	97.71	96.83	95.68	97.71	97.62	94.53	95.59	98.24	98.85	95.06	96.78±1.47
Precision	96.70	95.46	98.14	97.11	98.14	99.38	97.11	97.32	98.32	96.66	97.44±1.10
Sensitivity	97.91	97.06	92.25	97.52	96.36	89.09	92.90	98.54	98.94	92.05	95.26±3.40
Specificity	97.56	96.65	98.54	97.85	98.59	99.49	97.77	98.02	98.79	97.46	98.07±0.81
F1-score	97.30	96.26	95.10	97.31	97.24	93.96	94.96	97.93	98.63	94.30	96.34±1.66

Table 2 Comparison of different methods using the same amplitude-frequency-aware fusion features, but different classifiers, for the identification of the STN

Methods	Accuracy (%)	Precision (%)	Recall (%)	Specificity (%)	F1-score (%)	Test time (s)	P-value
DT	89.37±1.25	88.57±2.14	86.65±0.90	91.45±1.67	87.60±1.27	0.13	1.49e−12
SVM	90.76±1.41	91.03±2.23	87.89±2.22	93.10±1.62	89.41±1.67	0.11	1.93e−10
RF	91.77±2.14	92.35±3.33	88.88±2.52	94.15±2.46	90.56±2.52	0.16	6.29e−7
KNN	87.65±2.02	87.56±2.87	84.03±2.63	90.54±2.13	85.76±2.75	3.45	4.84e−10
CNN	93.99±2.80	95.88±3.51	90.78±2.56	96.94±2.35	93.26±4.21	1.55	1.7e−2
Ours	**96.78±1.47**	**97.44±1.10**	**95.26±3.40**	**98.07±0.81**	**96.34±1.66**	2.22	–

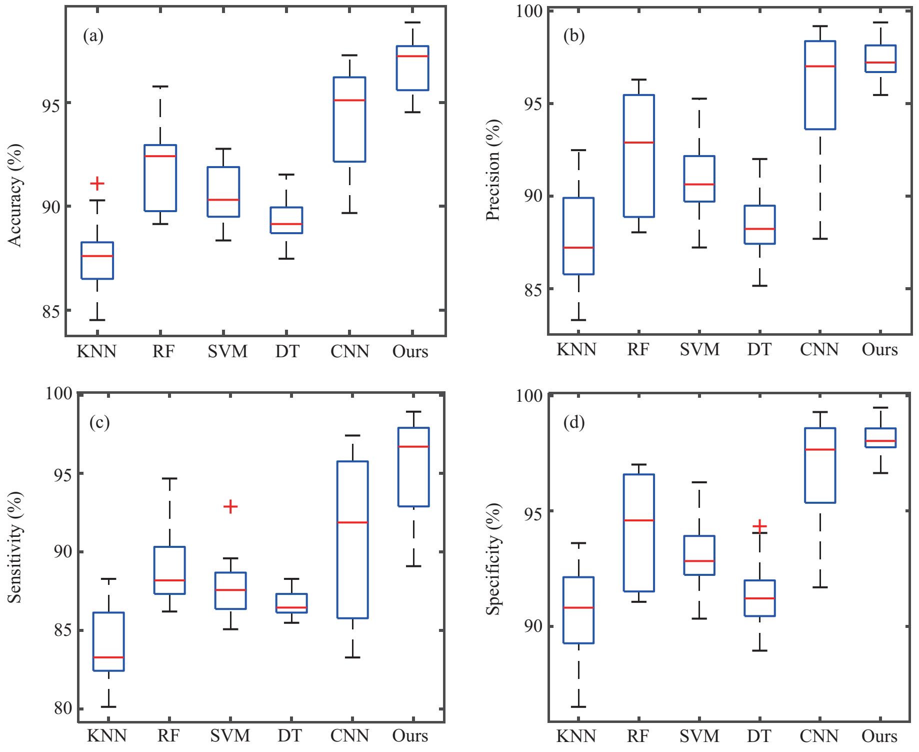

Figure 8 (Color online) The performance of different methods with the same amplitude-frequency-aware fusion features, but different classifiers for the identification of the STN. Performance metrics include: (a) accuracy, (b) precision, (c) sensitivity, and (d) specificity. The red line represents the median and the red + represents the outliers. The upper and lower boundaries of the blue box represent the upper and lower quartiles, respectively. The whiskers (i.e., error bars) represent the minimum and maximum values (except the outliers).

amplitude-frequency-aware deep fusion network method and a CBAM-integrated CNN model to identify the STN in order to accurately localize the electrode. In all comparison experiments, 10-fold cross-validation was conducted for training and validating these models. The results of the presented model, along with the corresponding 10-fold cross-validation, are shown in Table 1. The results are represented by the average values and standard deviations of the five evaluation criteria.

To evaluate the performance of the proposed method, two experiments were conducted, one on the classifiers and one on the feature extraction methods. For the first experiment, all comparison methods used the same amplitude-frequency-aware fusion features but used their own classifiers. From the results shown in Table 2 and Figure 8, it may be observed that the proposed method with the CBAM-integrated

Table 3 Comparison of different methods using the same classifiers, but different amplitude-frequency-aware fusion features, for the identification of the STN

Methods	Accuracy (%)	Precision (%)	Recall (%)	Specificity (%)	F1-score (%)	Test time (s)	P-value
CWT	92.68±1.62	93.07±2.31	89.99±2.88	94.84±1.43	91.50±2.57	2.19	1.80e−9
GASF	93.54±1.35	93.56±1.85	91.55±3.32	95.20±1.24	92.49±1.59	2.16	5.36e−7
Ours	**96.78±1.47**	**97.44±1.10**	**95.26±3.40**	**98.07±0.81**	**96.34±1.66**	2.22	–

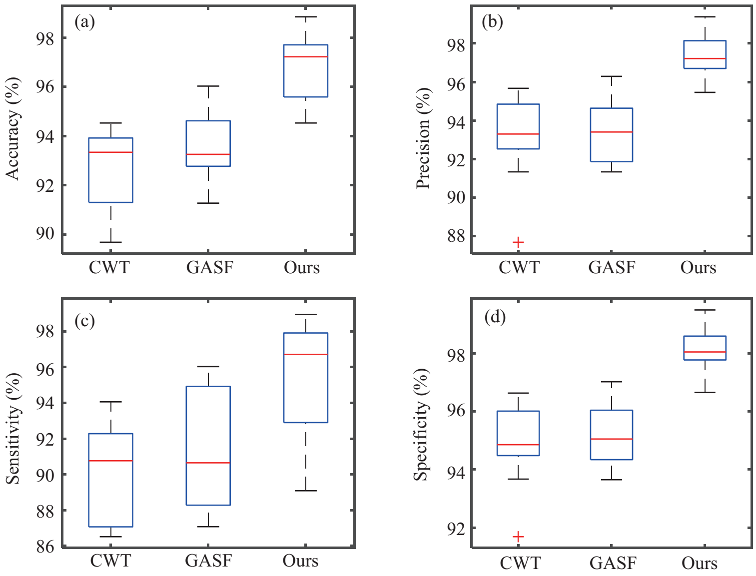

Figure 9 (Color online) The measurement performance of different methods with the same CBAM integrated CNN classifier, but different features, for the identification of the STN, including (a) accuracy, (b) precision, (c) sensitivity, and (d) specificity. The red line represents the median, and the red + represents the outliers. The upper and lower boundaries of the blue box represent the upper and lower quartiles, respectively. The whiskers (i.e., error bars) represent the minimum and maximum values (except the outliers).

CNN classifier performs better than the other methods. For the second experiment, all the methods used the same CBAM-integrated CNN classifier but used their own features. As shown in Table 3 and Figure 9, the average accuracy, precision, sensitivity, specificity, and F1-score of the proposed method were superior to those of the other methods.

In addition, a paired t-test was performed based on the accuracy metric of the proposed method and the other comparison methods, as shown in Tables 2 and 3. All P-values were less than 0.05, which indicates that the proposed method performed significantly better. The execution times of the conventional classification methods were shorter than that of the proposed method, as shown in Tables 2 and 3. However, the proposed method detected the STN more accurately, which is more important for clinicians than the execution time. As shown in Figure 10(a), the identification performance score of the proposed method was calculated as the mean of the five evaluation criteria. The proposed method scored higher than all the other methods.

Sweet spots detection analysis. Xiao et al. [18] proposed the first model to identify sweet spots for the selection of the optimal stimulated contact, by combining the amplitude sequence features GASF with the CBAM-enhanced network model. In contrast, this work employed an amplitude-frequency-aware deep fusion network and the classifier of the CBAM-integrated CNN model. As shown in Table 4, Figure 11, and Figure 10(b), based on the above five evaluation criteria, the classification performance of the proposed method for sweet spot detection outperformed the state-of-the-art method [18].

3.2 Qualitative analysis

In order to qualitatively evaluate the performance of the proposed method, 20 testing patients were randomly selected from the 100 PD patients, and the optimal stimulated contact determined by the proposed method was compared with that determined by the neurosurgeons, as shown in Figure 12. As shown in Figure 12, the sweet spot identification accuracy of the proposed method was 97.42%, fulfilling the clinical accuracy requirements. Furthermore, the proposed method accurately selected the optimally

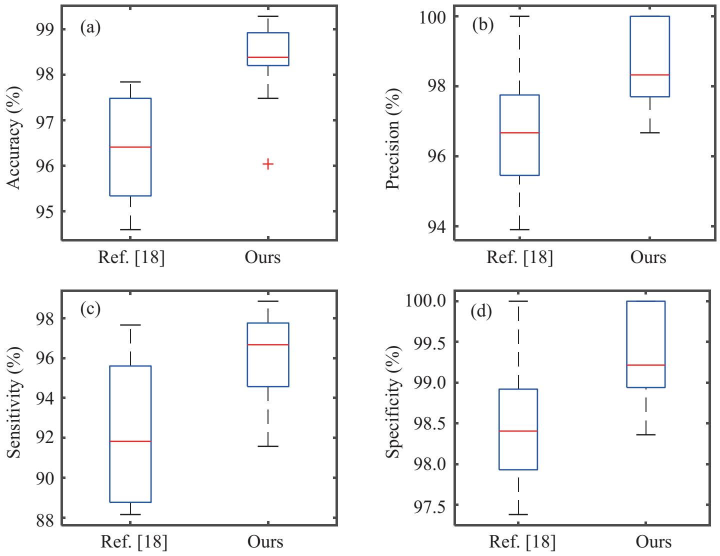

Figure 10 (Color online) The measurement performance of different methods for the identification of the sweet spots, including (a) accuracy, (b) precision, (c) sensitivity, and (d) specificity. The red line represents the median, and the red + represents the outliers. The upper and lower boundaries of the blue box represent the upper and lower quartiles, respectively. The whiskers (i.e., error bars) represent the minimum and maximum values (except the outliers).

Table 4 Comparison of different methods for identifying sweet spots

Methods	Accuracy (%)	Precision (%)	Sensitivity (%)	Specificity (%)	F1-score (%)	Test time (s)
Reference [18]	96.48±1.17	96.99±1.94	92.22±3.66	98.62±0.86	94.55±2.54	1.04
Ours	**98.24±0.92**	**98.53±1.19**	**96.05±2.11**	**99.31±0.57**	**97.28±1.52**	1.13

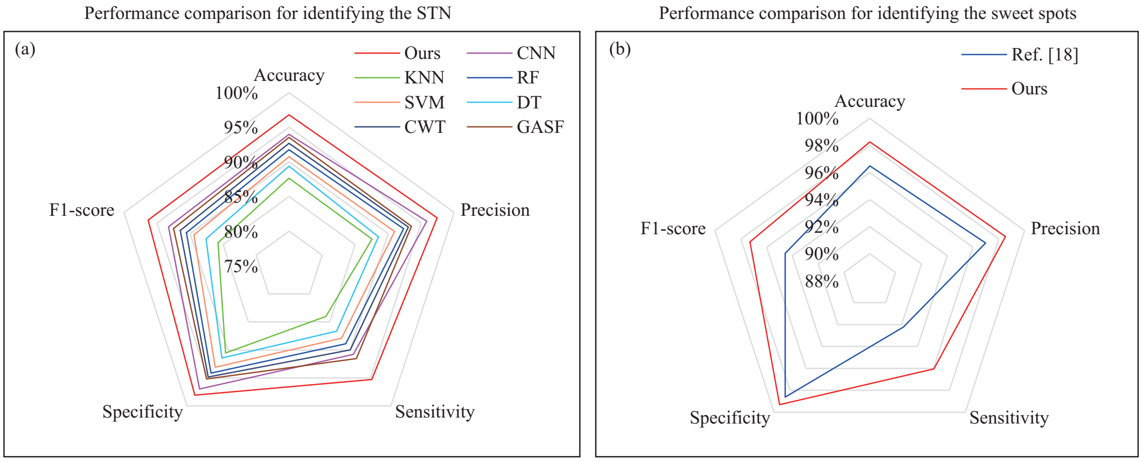

Figure 11 (Color online) The performance comparison results from different methods for the identification of the STN and sweet spots. (a) Comparison results for the identification of the STN; (b) comparison results for the identification of sweet spots. These comparison results were calculated according to the mean of the five evaluation criteria.

stimulated contacts for 18 out of 20 patients, with a 90% accuracy. In clinical practice, clinicians usually choose both the optimal and suboptimal contacts as the final candidate contacts. Following this practice, the proposed method reached 100% accuracy, satisfying the requirements of precise surgery. Therefore, the choices of the proposed method were consistent with those of the clinicians, and so, could provide useful guidance for neurosurgeons.

4 Discussion

When performing STN-DBS surgery, accurate stimulation of the patient-specific sensorimotor region is extremely important for the successful treatment of PD patients. In this study, an amplitude-frequency-

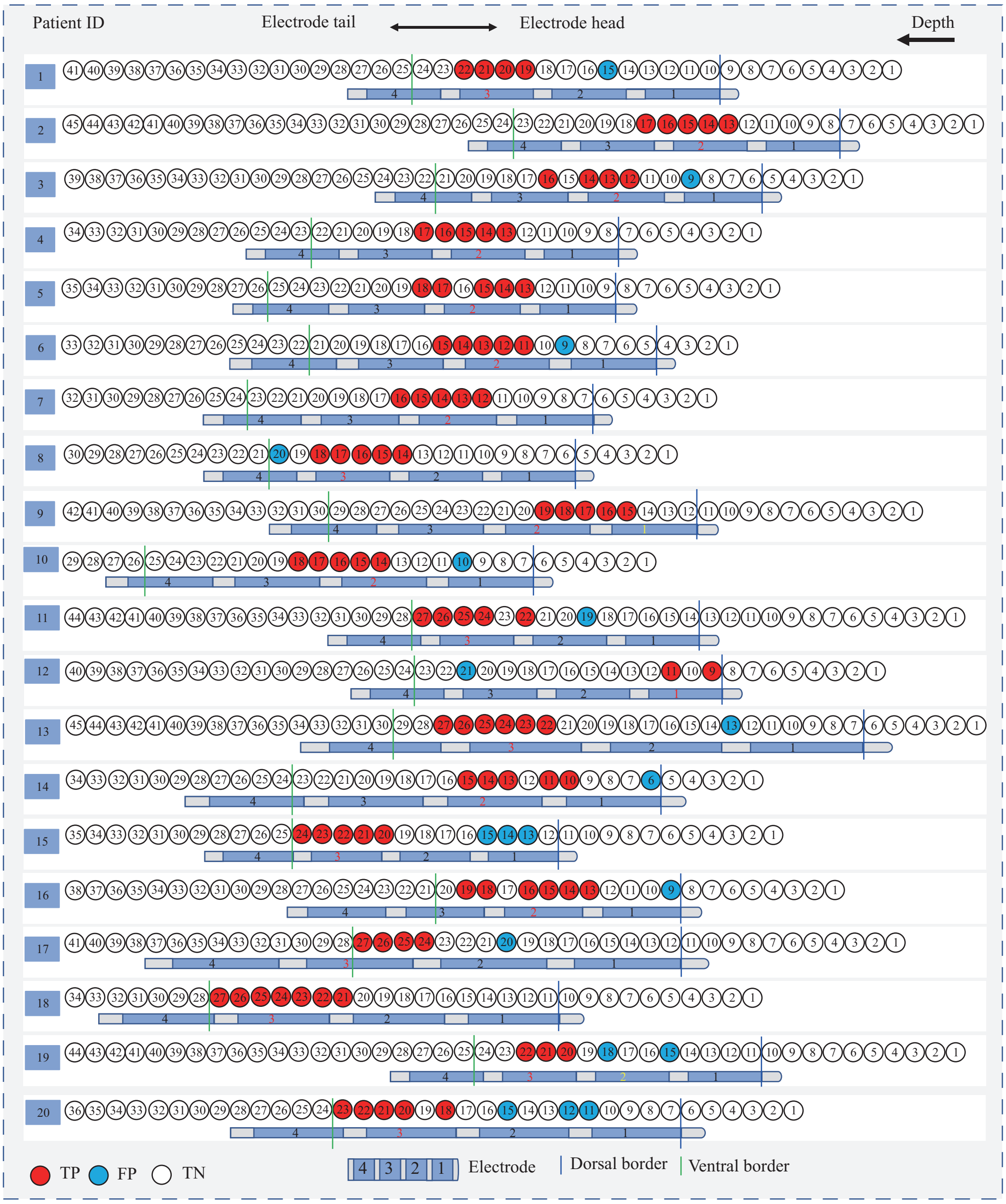

Figure 12 (Color online) Comparison of the sweet spots and contacts identified by neurosurgeons and the proposed model. Going from right to left along the horizontal axis, the depth (mm) of the implanted electrode increases from the dorsal border to the ventral border of the STN. The cannulas with stylets are usually lowered from 10.0 mm above the estimated target down below it. Microelectrode signals were captured every 0.5 mm, and the recording time was 1 s long. In practice, the actual step size was sometimes stretched according to the actual MERs signals, and the electrodes are visually scaled based on the electrode position. Each numbered circle represents the location of the MERs. The TP, FP, and TN electrodes are marked in red, blue, and white, respectively. The red contacts indicate the optimal stimulated contact determined by the proposed method, and the yellow contacts present the actual optimal stimulated contacts determined by clinicians, which were misidentified by the proposed method as non-optimal contact.

aware deep fusion network was proposed for optimal stimulated contact selection on STN-DBS electrodes. In contrast to traditional methods, this study procured an AI solution for the whole process of MERs signal analysis in STN-DBS surgery, including MERs monitoring, STN-DBS electrode positioning, and electrode contact selection.

Sweet spots are identified by the unique features of MERs, including the frequency and amplitude features. However, not all MERs signals have obvious high-frequency and high-amplitude features; some MERs signals only have these features in some fragments, which increases the difficulty of classifying

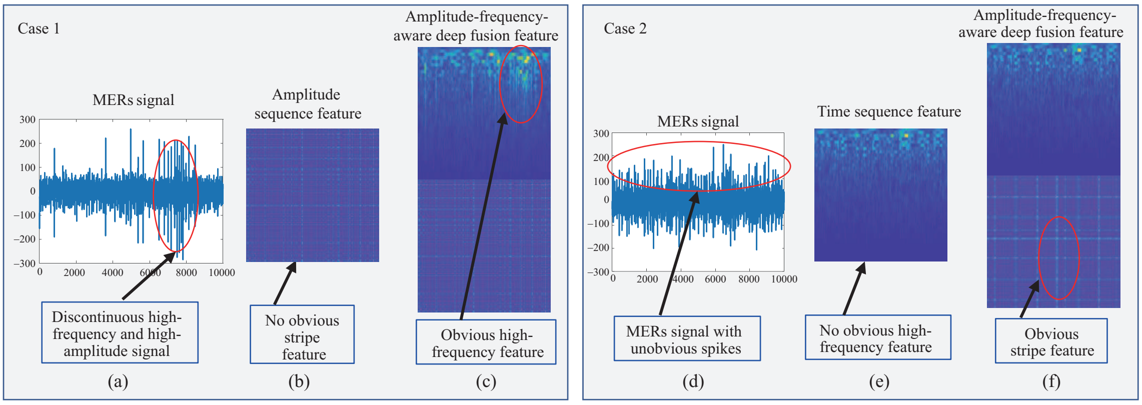

Figure 13 (Color online) The feature images generated from the amplitude sequence, time sequence, and amplitude-frequency-aware. In case 1, (a) raw MERs signals, (b) amplitude sequence features, and (c) amplitude-frequency-aware deep fusion feature. In case 2, (d) raw MERs signals, (e) time sequence feature, (f) amplitude sequence feature. The red ellipses represent the high-frequency and high-amplitude parts of the signals.

the MERs. Therefore, it was necessary to select an effective feature extraction method. As shown in Figures 13(a) and (b), because the MERs signal of case 1 was a discontinuous high-frequency and high-amplitude MERs signal, the GASF amplitude sequence feature extraction was not suitable owing to the lack of an obvious corresponding stripe feature. In this study, the amplitude-frequency-aware deep fusion feature extraction method was used, which combined the time sequence feature and amplitude sequence feature to identify MERs, as shown in Figure 13(c). This can identify the MERs according to the fusion time sequence feature labelled in red ellipses. In case 2, as shown in Figures 13(d) and (e), when the MERs signal consisted of the unobvious spike signals, the time sequence feature was unsuitable for identifying the MERs owing to the lack of obvious high-frequency features; in contrast, in the proposed method, the fusion amplitude sequence feature with the obvious stripe feature was used to identify the MERs signals, which are labelled in red ellipses of Figure 13(f). Importantly, GASF features were not suitable for discontinuous high-frequency and high-amplitude MERs signals, whereas the CWT feature extraction method was unsuitable for the MERs signals with unobvious spikes. However, the presented amplitude-frequency-aware deep fusion network could overcome these difficulties of the MERs signals with different grading frequencies and amplitudes for the identification of the STN and sweet spots.

Although the proposed method could identify the sweet spots from the MERs signals with high accuracy, clinicians determine the sweet spots in practice from more factors than just the MERs. The other factors are: (1) the patient's symptom improvement, including muscle tension and motor control, and (2) side effects, which should be avoided. The results for patients 9 and 10 shown in Figure 12 are examples of where relying on the MERs alone failed to identify the best contacts to stimulate. Therefore, in this study, two candidate contacts were selected, including the optimal and sub-optimal contacts. For doctors, the accuracy of the final contact selection reaches 100%, which can also shorten the surgical duration, lessen the suffering of patients, and reduce the dependence on the clinical experience.

Generally, the selection of optimal stimulated contact is a time-consuming and labor-intensive process for clinicians, who test individual contacts one at a time. With the development of more complex electrodes with multiple contacts [6], the selection of electrode contact will be even more difficult. This study identified the optimal stimulated contact according to the assumption "passing through sweet spots accumulation" [4], therefore, according to the analysis of the MERs signals from all directions, the proposed method can be more suitable for the complex electrodes with multiple contacts, especially for directional multipolar electrodes.

Although this present work can guide intraoperative sweet spot determination and postoperative optimal stimulated contact selection, this retrospective study was performed on the data from only one medical center. To promote the robustness and generalization of this study, the immediate plan is to conduct a retrospective analysis of data from multiple medical centers. Moreover, to achieve automatic decision-making for the entire process for STN-DBS surgeries, automatic preoperative intelligent nucleus segmentation and trajectory planning of electrode implantation will be developed.

5 Conclusion

This study proposed an amplitude-frequency-aware deep fusion network for optimal stimulated contact selection on STN-DBS electrodes. The proposed method first identified the STN and sweet spots using amplitude-frequency-aware fusion features to accurately localize the STN-DBS electrode. Then, the optimal electrode contact was selected according to the locations of the sweet spots. Experimental results demonstrated that the proposed method outperformed state-of-the-art methods for STN. Furthermore, the STN was identified with an average accuracy of 96.78%, the precision of 97.77%, the sensitivity of 95.26%, and the specificity of 98.07%, and the sweet spots were identified with an average accuracy of 98.24%, the precision of 98.53%, the sensitivity of 96.05%, and the specificity of 99.31%. The selected optimal stimulated contacts were consistent with the results of neurosurgeons' successful decisions, which demonstrates that the proposed method has great potential to improve surgical efficiency while reducing the dependence on clinicians' experience.

Acknowledgements This work was supported in part by Shenzhen Fundamental Research Program (Grant Nos. JCYJ20200109110208764, JCYJ20200109110420626), in part by National Natural Science Foundation of China (Grant Nos. U1813204, 61802385, 62072468), Natural Science Foundation of Guangdong (Grant No. 2021A1515012604), and in part by Guangdong Basic and Applied Basic Research Foundation (Grant No. 2019A1515111106). We gratefully thank the reviewers for their constructive comments.

References

1 Dorsey E R, Elbaz A, Nichols E, et al. Global, regional, and national burden of Parkinson's disease, 1990–2016: a systematic analysis for the global burden of disease study 2016. Lancet Neurol, 2018, 17: 939–953

2 Mann J M, Foote K D, Garvan C W, et al. Brain penetration effects of microelectrodes and DBS leads in STN or GPi. J Neurol Neurosurg Psychiatry, 2009, 80: 794–798

3 Schuepbach W M M, Rau J, Knudsen K, et al. Neurostimulation for Parkinson's disease with early motor complications. N Engl J Med, 2013, 368: 610–622

4 Boutet A, Madhavan R, Elias G J B, et al. Predicting optimal deep brain stimulation parameters for Parkinson's disease using functional MRI and machine learning. Nat Commun, 2021, 12: 1–13

5 Zhang F, Wang F, Li W G, et al. Relationship between electrode position of deep brain stimulation and motor symptoms of Parkinson's disease. BMC Neurol, 2021, 21: 122

6 Krauss J K, Lipsman N, Aziz T, et al. Technology of deep brain stimulation: current status and future directions. Nat Rev Neurol, 2021, 17: 75–87

7 Steigerwald F, Matthies C, Volkmann J. Directional deep brain stimulation. Neurotherapeutics, 2019, 16: 100–104

8 Lambert C, Zrinzo L, Nagy Z, et al. Confirmation of functional zones within the human subthalamic nucleus: patterns of connectivity and sub-parcellation using diffusion weighted imaging. NeuroImage, 2012, 60: 83–94

9 Plantinga B R, Temel Y, Duchin Y, et al. Individualized parcellation of the subthalamic nucleus in patients with Parkinson's disease with 7T MRI. NeuroImage, 2018, 168: 403–411

10 Pozzi N G, Arnulfo G, Canessa A, et al. Distinctive neuronal firing patterns in subterritories of the subthalamic nucleus. Clin NeuroPhysiol, 2016, 127: 3387–3393

11 Dembek T A, Roediger J, Horn A, et al. Probabilistic sweet spots predict motor outcome for deep brain stimulation in Parkinson disease. Ann Neurol, 2019, 86: 527–538

12 Novak P, Przybyszewski A W, Barborica A, et al. Localization of the subthalamic nucleus in Parkinson disease using multiunit activity. J Neurol Sci, 2011, 310: 44–49

13 Wan K R, Maszczyk T, See A A Q, et al. A review on microelectrode recording selection of features for machine learning in deep brain stimulation surgery for Parkinson's disease. Clin Neurophys, 2019, 130: 145–154

14 Karthick P A, Wan K R, Qi A S A, et al. Automated detection of subthalamic nucleus in deep brain stimulation surgery for Parkinson's disease using microelectrode recordings and wavelet packet features. J Neurosci Method, 2020, 343: 108826

15 Khosravi M, Atashzar S F, Gilmore G, et al. Intraoperative localization of STN during DBS surgery using a data-driven model. IEEE J Transl Eng Health Med, 2020, 8: 1–9

16 Thompson J A, Oukal S, Bergman H, et al. Semi-automated application for estimating subthalamic nucleus boundaries and optimal target selection for deep brain stimulation implantation surgery. J Neurosurg, 2019, 130: 1224–1233

17 Akram H, Sotiropoulos S N, Jbabdi S, et al. Subthalamic deep brain stimulation sweet spots and hyperdirect cortical connectivity in Parkinson's disease. NeuroImage, 2017, 158: 332–345

18 Xiao L X, Li C Z, Wang Y J, et al. Automatic identification of sweet spots from MERs for electrodes implantation in STN-DBS. Int J CARS, 2021, 16: 809–818

19 Wang Z, Oates T. Encoding time series as images for visual inspection and classification using tiled convolutional neural networks. In: Proceedings of the 27th AAAI Conference on Artificial Intelligence, 2015. 40–46

20 Nowacki A, Nguyen T A K, Tinkhauser G, et al. Accuracy of different three-dimensional subcortical human brain atlases for DBS-lead localisation. NeuroImage-Clin, 2018, 20: 868–874

21 Woo S, Park J, Lee J Y, et al. CBAM: convolutional block attention module. In: Proceedings of European Conference on Computer Vision (ECCV), 2018. 3–19

22 Cardona H D V, Álvarez M A, Orozco A. Multi-task learning for subthalamic nucleus identification in deep brain stimulation. Int J Mach Learn Cyber, 2018, 9: 1181–1192

23 Martin T, Peralta M, Gilmore G, et al. Extending convolutional neural networks for localizing the subthalamic nucleus from micro-electrode recordings in Parkinson's disease. BioMed Signal Process Control, 2021, 67: 102529

24 Rajpurohit V, Danish S F, Hargreaves E L, et al. Optimizing computational feature sets for subthalamic nucleus localization in DBS surgery with feature selection. Clin Neurophysiol, 2015, 126: 975–982

25 Valsky D, Marmor-Levin O, Deffains M, et al. Stop! border ahead: automatic detection of subthalamic exit during deep brain stimulation surgery. Mov Disord, 2017, 32: 70–79

26 Bruce L M, Koger C H, Li J. Dimensionality reduction of hyperspectral data using discrete wavelet transform feature extraction. IEEE Trans Geosci Remote Sens, 2002, 40: 2331–2338

27 Cheng Y W, Lin M X, Wu J, et al. Intelligent fault diagnosis of rotating machinery based on continuous wavelet transform-local binary convolutional neural network. Knowl-Based Syst, 2021, 216: 106796

28 Salyers J B, Dong Y, Gai Y. Continuous wavelet transform for decoding finger movements from single-channel EEG. IEEE Trans Biomed Eng, 2019, 66: 1588–1597

29 Kingma D P, Ba J. Adam: a method for stochastic optimization. In: Proceedings of the 3rd International Conference on Learning Representations, 2015